Near-IR response of highly-strained Si photodetector linking first principles and TCAD

Nicolas Roisin
ICTEAM
Université catholique de Louvain
Louvain-la-Neuve, Belgium
nicolas.roisin@uclouvain.be

Jean-Pierre Raskin
ICTEAM
Université catholique de Louvain
Louvain-la-Neuve, Belgium
jean-pierre.raskin@uclouvain.be

Denis Flandre
ICTEAM
Université catholique de Louvain
Louvain-la-Neuve, Belgium
denis.flandre@uclouvain.be

***Abstract*—TCAD finite element methods coupled with first-principles simulation are undertaken to predict the enhancement of the optoelectronic performance in highly-strained semiconductors. The increase of the absorption coefficient in strained silicon is first computed using first-principles theory and leads to significant improvement in the infrared spectrum. The absorption limit is moved from 1.1 µm wavelength in relaxed silicon to above 1.35 µm when 2% tensile strain is applied along the [110] crystal direction. A strained silicon photodetector with three thicknesses (1 µm, 10 µm and 50 µm) is then simulated using TCAD software to retrieve the strain-enhanced quantum efficiency. The results are compared to a theoretical model and show significant improvement. An increase from 0.03% to 1.92% (resp. 0.11% to 7.60%) is observed for 10 µm (resp. 50 µm) thickness at a photon wavelength of 1.2 µm. The combined approach of using TCAD tool to predict the performances of a novel photodetector for which the material properties have been computed using first principles brings new possibilities for the investigation of advanced devices.**

***Index Terms*—strain, silicon, first-principles, DFT, photodetector, TCAD, quantum efficiency**

I. Introduction

Silicon photodetectors are commonly used in visible light photodetection due to their high sensitivity and efficiency in converting photons into electrical signals. They are relatively easy to manufacture, can be produced in large quantities at low cost, and can be integrated with other electronic components, making them well-suited for use in a wide range of devices. The ability of silicon-based photodetectors to detect longer-wavelength infrared radiation beyond 1.1 µm is limited due to the 1.12 eV band gap of the material [1]. To overcome these limitations, the preferred solutions require the use of lower band gap materials such as Ge [2] or InGaAs [3]. However, highly-strained silicon emerges as a promising candidate for near-infrared applications thanks to the strain dependence of its optical properties [4] and the high strain level ($\sim$3.5%) achieved in previous work [5].

TCAD simulation allows for the detailed analysis of the physical processes that occur in semiconductors, such as light absorption, carrier generation, recombination and transport. These analyses are crucial to optimize device performances such as efficiency, sensitivity or response time. Experimentally-based models are needed but new material or advanced physical effects remain a challenge to be correctly tackled. On the opposite, first-principles study based on density-functional theory (DFT) is a powerful tool to predict advanced material properties, including the electronic structure [6], lattice vibrations [7] and the phonon-assisted absorption [8].

This work predicts the optical performance, i.e. quantum efficiency, of a highly-strained silicon photodetector based on p-i-n diode configuration using TCAD simulation. The stress-related material properties needed for the finite-elements simulation are provided by first-principles calculations coupled with an analytical expression of the absorption coefficient. Section II describes the methods to compute the strained-silicon properties and the device efficiency. Results are then presented and discussed in section III.

II. Materials and methods

A. First-principles study for strained silicon

The theoretical analysis is performed to retrieve the absorption coefficient of highly-strained silicon in the [110] crystal direction based on the band gaps, effective masses and phonon energies. The first-principles analysis of the absorption is an extension up to 4% strain of a previous work [4].

The key parameters are computed from first principles using density-functional (DFT) theory to retrieve the band structure and effective masses and density-functional perturbation theory (DFPT) to retrieve the phonon energies, as implemented in ABINIT [9], [10] with the generalized-gradient approximation (GGA) from Perdew–Burke–Ernzerhof (PBE) [11].

A structure relaxation is first realized for each strain level to retrieve the position of the two silicon atoms within the strained primitive unit cell. The band structure is then determined using a 18x18x18 Monkhorst-Pack **k**-point grid [12] with a plane-wave cut-off of 20 Hartree. The well-known band gap underestimation is corrected by applying scissor shifts to the conduction band in order to fit the experimental gaps of relaxed silicon.

The modification of the silicon lattice under stress conditions along the [110] crystal direction is given by the strain tensor

$$\mathbf{E}_{[110]} = \frac{1}{2}\begin{pmatrix} (\varepsilon_\perp + \varepsilon_\parallel) & (\varepsilon_\perp - \varepsilon_\parallel) & 0 \\ (\varepsilon_\perp - \varepsilon_\parallel) & (\varepsilon_\perp + \varepsilon_\parallel) & 0 \\ 0 & 0 & 2\varepsilon_\perp \end{pmatrix}, \quad (1)$$

where $\varepsilon_\perp$ is the strain in the [110] direction. The associated transverse component $\varepsilon_\parallel$ is given by

$$\varepsilon_\parallel = -\nu_{[110]}\ \varepsilon_\perp, \tag{2}$$

with the Poisson ratio

$$\nu_{[110]} = \frac{4C_{12}C_{44}}{2C_{11}C_{44} + (C_{11}+2C_{12})(C_{11}-C_{12})} \tag{3}$$

where $C_{11} = 165.77$ GPa, $C_{12} = 63.93$ GPa, and $C_{44} = 79.62$ GPa are the elastic constants of silicon [13].

The density-of-states effective mass of a given band (conduction or valence) is defined as the one giving the same density of states as if the band was parabolic. In the case of the valence band, it is obtained through

$$\frac{\sqrt{\pi}}{2}\frac{1}{2\pi^2}\left(\frac{2m_v}{\hbar^2}\right)^{3/2}(k_BT)^{3/2} = \int_{-\infty}^{E_v} g(E)\exp\left(-\frac{E_v-E}{k_BT}\right)dE, \tag{4}$$

where E_v is the energy of the valence band maximum and $g(E)$ is the density of states obtained for each strained configuration. A similar expression holds for the conduction band. The parameters computed are then injected in an analytical expression of the absorption coefficient [14] taking into account the possible routes for the photon absorption:

$$\begin{aligned}\alpha_{\mathbf{q}\nu} = \ & \frac{AN_{\text{val}}}{E_\lambda\hbar\omega_{\mathbf{q}\nu}} \Big[\frac{N_{\mathbf{q}}(E_\lambda-E_g+\hbar\omega_{\mathbf{q}\nu})^2}{|E_{g1}-E_\lambda-i\Gamma_d|^2}H(E_\lambda-E_g+\hbar\omega_{\mathbf{q}\nu}) \\ & + \frac{(N_{\mathbf{q}}+1)(E_\lambda-E_g-\hbar\omega_{\mathbf{q}\nu})^2}{|E_{g1}-E_\lambda-i\Gamma_d|^2}H(E_\lambda-E_g-\hbar\omega_{\mathbf{q}\nu}) \\ & + \frac{N_{\mathbf{q}}(E_\lambda-E_g+\hbar\omega_{\mathbf{q}\nu})^2}{|E_{g2}-E_\lambda-i\Gamma_d|^2}H(E_\lambda-E_g+\hbar\omega_{\mathbf{q}\nu}) \\ & + \frac{(N_{\mathbf{q}}+1)(E_\lambda-E_g-\hbar\omega_{\mathbf{q}\nu})^2}{|E_{g2}-E_\lambda-i\Gamma_d|^2}H(E_\lambda-E_g-\hbar\omega_{\mathbf{q}\nu})\Big],\end{aligned} \tag{5}$$

where $\mathbf{q}\nu$ stands for the phonon mode ν at symmetry point $\mathbf{q}$, N_{val} is the number of degenerated conduction valleys, E_g is the indirect band gap, E_{g1} and E_{g2} are the direct band gap energies providing intermediate states, Γ_d is a damping factor, and

$$N_{\mathbf{q}} = \left(\exp\left(\frac{\hbar\omega_{\mathbf{q}\nu}}{k_BT}\right)-1\right)^{-1} \tag{6}$$

is the Bose-Einstein distribution for the number of phonons of frequency $\omega_{\mathbf{q}\nu}$. The material-dependent proportionality constant A is defined as

$$A = \frac{e^2 m_c^{3/2} m_v^{3/2} E_p D_{\mathbf{q}\nu}^2}{96\pi^2\hbar^3 m_0 c\varepsilon_0 n_r \rho_L}, \tag{7}$$

where e is the electron charge, m_0 is the free electron mass, c is the speed of light in vacuum, ρ_L is the material density, n_r is the refractive index, E_p is an energy parameter for the electron-photon interactions, $D_{\mathbf{q}\nu}$ is the phonon deformation potential for phonon mode ν at symmetry point $\mathbf{q}$, and m_c and m_v denote the density-of-states effective masses of the conduction and valence bands, respectively.

TABLE I

PHYSICAL PARAMETERS USED TO COMPUTE THE INDIRECT ABSORPTION COEFFICIENT OF RELAXED SILICON. THE PHONON DEFORMATION POTENTIALS ($D_{\mathbf{q}\nu}$) ARE GIVEN FOR THE THREE PHONON MODES (TA,TO AND LO) AT THE POSITION OF THE ELECTRON VALLEYS (Δ).

Parameters	Value	Parameters	Value
n_r	3.42	$E_{g,1}$	3.2 eV
ρ_L	2.328 g/cm^3	$E_{g,2}$	4 eV
m_c	$0.36\,m_0$	E_g	1.12 eV
m_v	$0.81\,m_0$	$D_{\text{TA},\Delta}$	4.1×10^8 eV/cm
T	300 K	$D_{\text{TO},\Delta}$	1.2×10^9 eV/cm
E_p	12 eV	$D_{\text{LO},\Delta}$	2.2×10^9 eV/cm
Γ_d	1.35 eV		

B. TCAD for photodetector simulation

Silvaco Atlas software is used to simulate the optical performance, i.e. external quantum efficiency, of a basic lateral silicon photodetector under stress conditions. The detector structure consists of 2 µm-long aluminium-contacted p- and n-type regions in a lightly doped p-well as displayed in Fig. 1. The width of the device is set to 20 µm while three thicknesses are studied (1, 10 and 50 µm). An anode and cathode Gaussian doping profiles with a peak value at the top surface of 10^{18} cm^{-3} and a deviation of 0.5 µm are chosen. The uniform intrinsic doping level of the p-well is set to 10^{15} cm^{-3}. An anti-reflection coating is added on top of the structure and a reflective layer at the bottom.

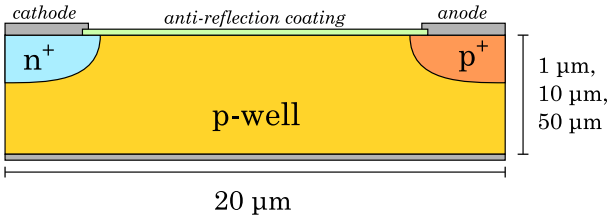

Fig. 1. Structure of the simulated p-i-n photodetector. Higher doping regions n^+ and p^+ are defined at the edge of a low-doped region (p-well) of 20 µm-long. An anti-reflection coating is added on top of the structure and a reflection layer at the bottom. Aluminium contacts of 2 µm-long are made at the cathode (n-side) and anode (p-side) of the diode structure. Three device thicknesses are studied: 1, 10 and 50 µm.

The simulated quantum efficiency is compared to the theoretical expression [15] by assuming ideal internal quantum efficiency:

$$\eta(\lambda) = \eta_i(\lambda)\frac{(1-r_1)}{1-r_1r_2e^{-2\alpha(\lambda)t}}[(1+r_2e^{-\alpha(\lambda)t})(1-e^{-\alpha(\lambda)t})] \tag{8}$$

where η_i is the internal quantum efficiency, λ is the photon wavelength, t is the thickness of the device, α is the absorption coefficient, r_1 and r_2 are respectively the reflection coefficients at the top and bottom interfaces. The anti-reflection coating and the reflective layer are supposed quasi-ideal, leading to $r_1 \approx 0$ and $r_2 \approx 1$, respectively.

III. Results and Discussion

A. Material parameters of strained silicon

The electron valleys (Δ), defined at the minima of the conduction bands, are six-fold degenerated along the <001> directions. At these positions, the band gap around 0.57 eV determined using the PBE functional is raised up to 1.12 eV with the scissor correction to fit the experimental value [16].

When a tensile strain along the [110] direction is applied, the broken symmetries of the crystal lift the degeneracy of the valleys into the Δ_2-valleys along the [001] and [00$\bar{1}$] directions and the Δ_4-valleys along [100], [010], [$\bar{1}$00] and [0$\bar{1}$0] directions. The gap energy decreases to 0.57 eV at 4% for the Δ_2 valleys and 1.04 eV for the Δ_4 valleys, as displayed in Fig 2.

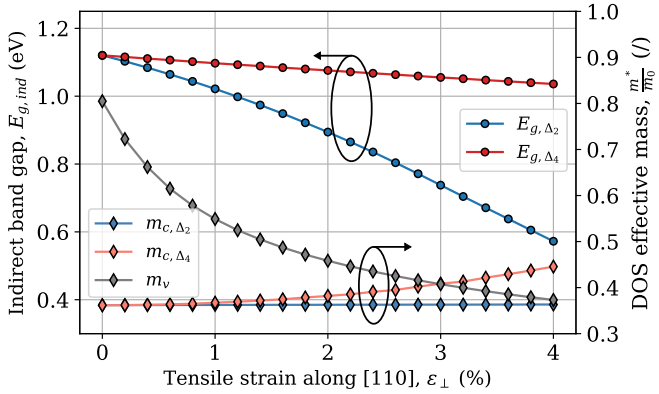

Fig. 2. Band gap reduction and density-of-states effective masses variations with regards to the tensile strain along [110] crystal direction. The band gap values (E_{g,Δ_2} and E_{g,Δ_4}) are read on the left axis while the valence (m_{c,Δ_2} and m_{c,Δ_4}) and conduction (m_v) effective masses are read on the right one. The indices Δ_2 and Δ_4 referred to the two types of electron valleys that split under stress conditions.

The conduction effective mass of the lower electron valleys (Δ_2) hardly presents any variations while the effective mass of the Δ_4 valleys rises from 0.36 m_0 to 0.45 m_0 under 4% strain, where m_0 is the electron mass. The valence effective mass shows higher variation with a reduction from 0.81 m_0 to 0.38 m_0. The results for the phonons energies at the Δ_2-valley position are displayed in Fig. 3. The changes in phonon frequencies are overall small, and these changes only have a limited impact on the absorption coefficient of highly-strained silicon.

Once the parameters are calculated, the absorption coefficient can be computed using relation Eq.(5). The absorption contributions are computed for each valley and added up. The effect of the variations in the conduction and valence effective masses is found in the proportional constant A (cfr. Eq.(7)) while the band gap reduction directly extends the absorption range. The absorption coefficients are displayed in Fig.4. The effect of the strain is significant at low absorption levels where the reduction of the band gap caused an important increase in the lower-energy photons that can be absorbed. The results in the absence of strain are compared to experimental

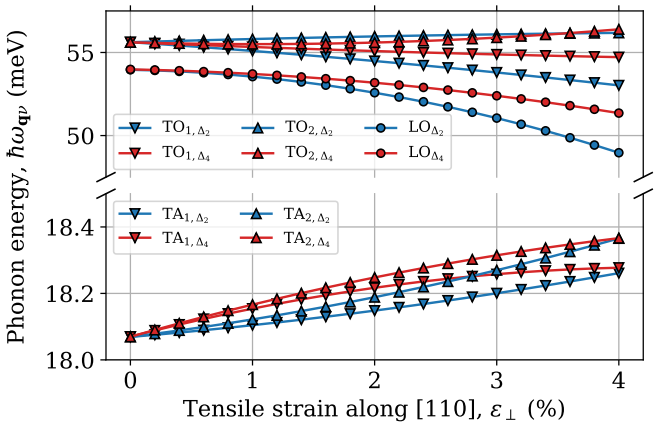

Fig. 3. Evolution of the optical and acoustic phonons energies for silicon crystal under tensile strain along the [110] direction. The indices Δ_2 and Δ_4 referred to the two types of electron valleys that split under stress conditions.

measurements [17] and show good agreement. At 4% strain, an extension of the cut-off wavelength from 1.15 µm to 2.13 µm is observed. While the absorption coefficient increase from 1 cm^{-1} to 245 cm^{-1} for a photon wavelength around 1.15 µm.

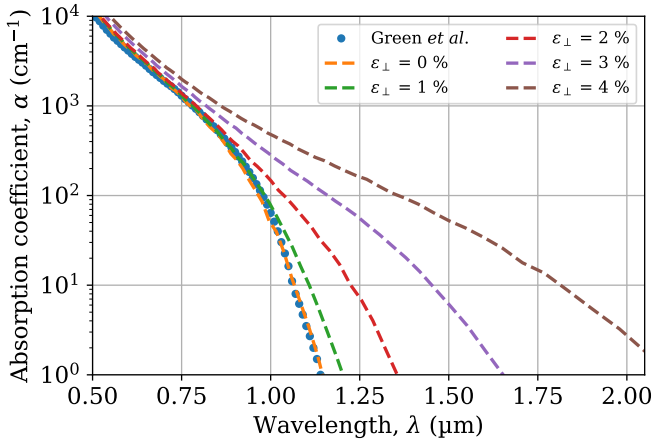

Fig. 4. Absorption coefficient spectrum of silicon for different levels of tensile strain applied in the [110] direction. The curve for the relaxed case is compared to experimental measurements (blue dots).

B. Quantum efficiency of strained-silicon device

The quantum efficiency is computed for an unpolarized light with normal incidence to the detector top surface. The complex refractive index taking into account the absorption coefficient of strained silicon is injected into the finite element simulation. Front and back reflections are enabled as well as trap-assisted recombination mechanisms (Shockley-Read-Hall).

Fig.5 shows the results of the quantum efficiency of the strained photodetector using TCAD simulation. The results are compared to the theoretical curves computed with Eq.(8) by assuming an ideal internal quantum efficiency. The reduction in the quantum efficiency between the theoretical and simulated curves comes from the additional recombination

mechanisms tackled by the finite element analysis and limiting the internal quantum efficiency.

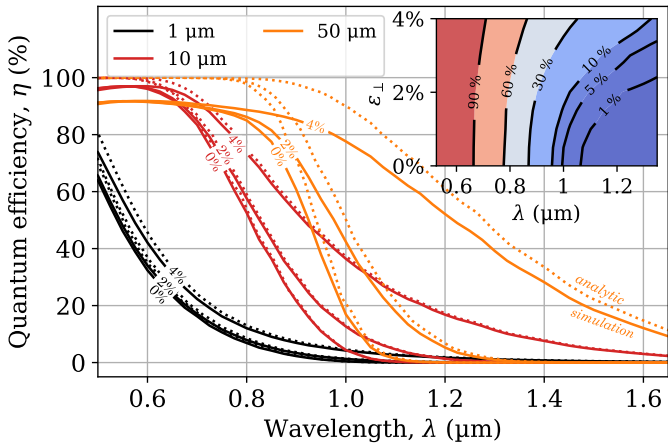

Fig. 5. Quantum efficiency computed by simulation using finite-elements software (continuous) and theoretically using Eq.(8) (dotted) for 0%, 2% and 4% tensile strain and thicknesses of 1 µm (black), 10 µm (red) and 50 µm (orange). The inset represents a map of the quantum efficiency for a thickness of 10 µm according to the strain and photon wavelength.

Three thicknesses, 1 µm, 10 µm and 50 µm, are considered in this study. Sufficient thickness is indeed needed for the low absorption processes where the effect of the applied stress is the highest. The external quantum efficiency at 1.2 µm increases from 0.03% (resp. 0.11%) to 18.50% (resp. 55.50%) for a 10 µm (resp. 50 µm)-thick device strained at 4%. At 2% strain level, a 5% quantum efficiency is achieved up to 1.075 µm (resp. 1.2 µm) for 10-µm (resp. 50 µm) thick device. On the opposite, the tensile strain in thin films of 1 µm does not enhance much the efficiency.

IV. Conclusion

A combined method based on theoretical computations of material properties injected in TCAD simulation has been applied for a highly-strained silicon photodetector. The absorption shows significant improvement in the near-infrared region by extending the detection limits beyond 2 µm and increasing by two orders of magnitude (from 1 cm^{-1} to 245 cm^{-1}) at the 1.15 µm wavelength for silicon strained up to 4%. The quantum efficiency, predicted by TCAD simulation, presents a significant improvement, especially for thicker devices (50 µm) with a quantum efficiency of 10% at a wavelength of 1.6 µm and 4% strain.

We have shown that the impact of strain is significant for the optical performance of a p-i-n photodetector which makes silicon strain engineering particularly interesting for infrared applications. The method presented with first-principles theory used in conjunction with TCAD software brings new capabilities for the analysis of advanced photodetector for which the material properties have not been correctly measured yet.

Acknowledgment

Computational resources have been provided by the supercomputing facilities of the Université catholique de Louvain (CISM/UCL) and the Consortium des Équipements de Calcul Intensif en Fédération Wallonie Bruxelles (CÉCI) funded by the Fond de la Recherche Scientifique de Belgique (F.R.S.-FNRS) under convention 2.5020.11 and by the Walloon Region.

References

[1] H. Lin, Z. Luo, T. Gu, L. C. Kimerling, K. Wada, A. Agarwal, and J. Hu, "Mid-infrared integrated photonics on silicon: a perspective," *Nanophotonics*, vol. 7, no. 2, pp. 393–420, 2017.

[2] I. A. Fischer, M. Brehm, M. De Seta, G. Isella, D. J. Paul, M. Virgilio, and G. Capellini, "On-chip infrared photonics with Si-Ge-heterostructures: What is next?" *APL Photonics*, vol. 7, no. 5, may 2022. [Online]. Available: https://doi.org/10.1063/5.0078608 https://aip.scitation.org/doi/10.1063/5.0078608

[3] X. Li, J. Zhang, C. Yue, X. Tang, Z. Gao, Y. Jiang, C. Du, Z. Deng, H. Jia, W. Wang, and H. Chen, "High performance visible-SWIR flexible photodetector based on large-area InGaAs/InP PIN structure," *Scientific Reports*, vol. 12, no. 1, may 2022. [Online]. Available: https://doi.org/10.1038/s41598-022-11946-7 https://www.nature.com/articles/s41598-022-11946-7

[4] N. Roisin, G. Brunin, G.-M. Rignanese, D. Flandre, and J.-P. Raskin, "Indirect light absorption model for highly strained silicon infrared sensors," *Journal of Applied Physics*, vol. 130, no. 5, aug 2021. [Online]. Available: https://aip.scitation.org/doi/10.1063/5.0057350

[5] A. K. Katiyar, K. Y. Thai, W. S. Yun, J. D. Lee, and J. H. Ahn, "Breaking the absorption limit of Si toward SWIR wavelength range via strain engineering," *Science Advances*, vol. 6, no. 31, pp. 1–11, 2020.

[6] M. Bouhassoune and A. Schindlmayr, "Ab initio study of strain effects on the quasiparticle bands and effective masses in silicon," *Advances in Condensed Matter Physics*, vol. 2015, 2015.

[7] N. Roisin, M. S. Colla, J. P. Raskin, and D. Flandre, "Raman strain–shift measurements and prediction from first-principles in highly strained silicon," *Journal of Materials Science: Materials in Electronics*, vol. 34, no. 5, 2023.

[8] J. Noffsinger, E. Kioupakis, C. G. Van de Walle, S. G. Louie, and M. L. Cohen, "Phonon-assisted optical absorption in silicon from first principles," *Physical Review Letters*, vol. 108, no. 16, p. 167402, 2012.

[9] X. Gonze, B. Amadon, G. Antonius, F. Arnardi, L. Baguet, J.-M. Beuken, J. Bieder, F. Bottin, J. Bouchet, E. Bousquet *et al.*, "The abinit project: Impact, environment and recent developments," *Computer Physics Communications*, vol. 248, p. 107042, 2020.

[10] A. H. Romero, D. C. Allan, B. Amadon, G. Antonius, T. Applencourt, L. Baguet, J. Bieder, F. Bottin, J. Bouchet, E. Bousquet *et al.*, "Abinit: Overview and focus on selected capabilities," *The Journal of chemical physics*, vol. 152, no. 12, p. 124102, 2020.

[11] J. P. Perdew, K. Burke, and M. Ernzerhof, "Generalized Gradient Approximation Made Simple," *Physical Review Letters*, vol. 77, no. 18, pp. 3865–3868, oct 1996. [Online]. Available: https://link.aps.org/doi/10.1103/PhysRevLett.77.3865

[12] H. J. Monkhorst and J. D. Pack, "Special points for brillouin-zone integrations," *Physical Review B*, vol. 13, no. 12, p. 5188, 1976.

[13] O. Madelung, *Semiconductors*, ser. Data in Science and Technology, O. Madelung, Ed. Berlin, Heidelberg: Springer Berlin Heidelberg, 1991. [Online]. Available: http://link.springer.com/10.1007/978-3-642-45681-7 https://link.springer.com/10.1007/978-3-642-45681-7

[14] C.-Y. Tsai, "Absorption coefficients of silicon: A theoretical treatment," *Journal of Applied Physics*, vol. 123, no. 18, p. 183103, 2018.

[15] T. Markvart and L. Castañer, "Chapter ia-1 - principles of solar cell operation," in *Practical Handbook of Photovoltaics (Second Edition)*, second edition ed., A. McEvoy, T. Markvart, and L. Castañer, Eds. Boston: Academic Press, 2012, pp. 7–31. [Online]. Available: https://www.sciencedirect.com/science/article/pii/B9780123859341000015

[16] W. Bludau, A. Onton, and W. Heinke, "Temperature dependence of the band gap of silicon," *Journal of Applied Physics*, vol. 45, no. 4, pp. 1846–1848, apr 1974. [Online]. Available: https://link.aps.org/doi/10.1103/PhysRevB.19.6620 http://aip.scitation.org/doi/10.1063/1.1663501

[17] M. A. Green and M. J. Keevers, "Optical properties of intrinsic silicon at 300 k," *Progress in Photovoltaics: Research and Applications*, vol. 3, no. 3, pp. 189–192, 1995.